ARTICLES
https://doi.org/10.1038/s41566-020-00707-5

nature photonics

High-power portable terahertz laser systems

Ali Khalatpour[1], Andrew K. Paulsen[1], Chris Deimert[2], Zbig R. Wasilewski[2,3,4,5] and Qing Hu[1]✉

Terahertz (THz) frequencies remain among the least utilized in the electromagnetic spectrum, largely due to the lack of powerful and compact sources. The invention of THz quantum cascade lasers (QCLs) was a major breakthrough to bridge the so-called 'THz gap' between semiconductor electronic and photonic sources. However, their demanding cooling requirement has confined the technology to a laboratory environment. A portable and high-power THz laser system will have a qualitative impact on applications in medical imaging, communications, quality control, security and biochemistry. Here, by adopting a design strategy that achieves a clean three-level system, we have developed THz QCLs (at ~4 THz) with a maximum operating temperature of 250 K. The high operating temperature enables portable THz systems to perform real-time imaging with a room-temperature THz camera, as well as fast spectral measurements with a room-temperature detector.

The terahertz (THz) spectral range (~1–10 THz) is a fertile ground for many applications[1]. For example, in biochemistry, THz applications have been developed to explore the bioactivity of chemical compounds and identify protein structures[2,3]. In astrophysics, there is a plan to launch a suborbital THz observatory, named GUSTO (Galactic/Extragalactic Ultra long Duration Balloon Spectroscopic-Stratospheric Terahertz Observatory), in 2021[4]. Neutral atomic oxygen was detected in the Martian atmosphere in 2014 using the high-frequency channel of the far-infrared heterodyne spectrometer GREAT (German Receiver for Astronomy at Terahertz Frequencies) on board SOFIA (Stratospheric Observatory for Infrared Astronomy)[5]. Although there is broad interest in THz imaging systems, the lack of portable high-power THz sources has prohibited applications in which the imaging subject is not movable to a laboratory environment. For security and public safety applications, many explosives (for example, C-4, HMX, RDX and TNT) and illegal drugs (for example, methamphetamine and heroin) have characteristic features in the THz range[6], but the detection must be carried out outside of a laboratory environment. With portable systems, THz imaging could also become a valuable tool for non-destructive testing, process control and quality inspection[7]. In medical applications, THz systems have been demonstrated to be highly effective in cancer imaging[1,8]. In particular, skin cancer is the most common form of cancer in the United States and early detection is key for a higher survival rate. A portable real-time THz imaging system used during regular health checkups can assist early detection and therefore significantly reduce fatalities. THz radiation may also play an important role in active demethylation for cancer therapy because the characteristic frequency of the methylated DNA falls in the THz region[9]. For this application, much greater average power is required than that used in linear THz spectroscopy.

The THz spectral range has historically been underdeveloped, as it lies in the gap between frequency ranges that are easily accessible with conventional semiconductor devices. At the low end, electronic devices such as transistors and frequency multipliers work well, but their power levels drop off precipitously above ~1 THz. Higher frequencies can be accessed by conventional semiconductor photonic devices such as diode lasers, but they are limited to >10 THz by the minimum bandgap energy of semiconductor host materials. The range of frequencies in the middle, ~1–10 THz, is the so-called THz gap. The invention of THz quantum cascade lasers (QCLs) held great promise to bridge this gap[10]. However, the demanding cooling requirements for THz QCLs have been a showstopper for achieving compact and portable systems, confining THz QCL systems to the laboratory environment. Therefore, raising the maximum operating temperature T_{max} to above that of a compact cooler (>235 K for single-stage thermoelectric coolers), or even no cooler at all, has been a paramount long-term goal in the field.

Both narrowband and broadband THz radiation can be generated at room temperature using frequency conversions. Narrowband THz radiation can be generated using semiconductor devices, either upconversion from electronic sources[11,12] or downconversion from higher-frequency laser sources[13–15]. Broadband THz radiation can be generated with downconversion from a mode-locked laser, using either photoconductive antennas[16,17] or optical rectification in nonlinear materials[18]. However, as fundamental oscillators, THz QCLs can generate much greater output power levels (>1 W)[19,20] and achieve much greater continuous-wave (c.w.) power efficiencies (>1%)[21]. Furthermore, broadband THz QCL gain media can be developed in other devices such as THz laser frequency combs[22,23] and radiation amplifiers[24].

Results and discussion

After the initial rapid increase of THz QCL T_{max} achieved during the period 2002–2005[10,25], progress slowed, eventually stalling in 2012 where the record remained at 200 K (ref. [26]) until 2019, when T_{max} = 210 K was achieved[27]. This slow and stagnant improvement in T_{max} begs the question whether there is a fundamental physical reason that THz QCLs cannot be operated significantly above 200 K. During the long stretch from 2002 to 2018, all T_{max} records were achieved using GaAs/AlGaAs active regions with relatively low barriers of $Al_{0.15}Ga_{0.85}As$. In an insightful discovery[28], it was found unambiguously that carrier leakage over these barriers becomes dominant at high temperatures. To suppress this leakage, higher barriers with an Al composition greater than 15% are needed. Previously, only scattered efforts were made to explore these taller barriers, but they all yielded inferior T_{max} compared to devices made with $Al_{0.15}Ga_{0.85}As$ barriers. The prevailing conclusion then was that

[1]Department of Electrical Engineering and Computer Science and Research Laboratory of Electronics, Massachusetts Institute of Technology, Cambridge, MA, USA. [2]Department of Electrical and Computer Engineering, University of Waterloo, Waterloo, Ontario, Canada. [3]Department of Physics and Astronomy, University of Waterloo, Waterloo, Ontario, Canada. [4]Waterloo Institute for Nanotechnology, University of Waterloo, Waterloo, Ontario, Canada. [5]Institute for Quantum Computing, University of Waterloo, Waterloo, Ontario, Canada. ✉e-mail: qhu@mit.edu

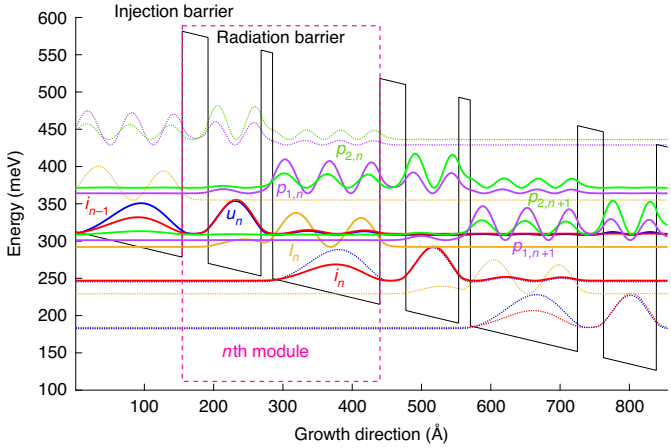

Fig. 1 | Probability density functions of subband states in a THz QCL with two quantum wells per module in the active region. The dashed box encloses one module. Important levels, both the desired three levels in one module and levels that may cause carrier leakage, are highlighted with thick lines.

the increased alloy and interface roughness scattering associated with taller barriers was detrimental to device performance, and therefore barriers with higher Al composition should be avoided. Later, it was found that these tall barrier devices had a previously overlooked leakage channel at elevated temperatures via their higher bound state(s)[29]. By careful engineering to minimize this leakage channel, devices with $Al_{0.3}Ga_{0.7}As$ barriers preserved desirable nonlinear current–voltage characteristics (distinguished by a negative differential resistance (NDR)) even at room temperature. All the previous THz QCLs showed almost linear current–voltage characteristics at room temperature, suggesting many leakage channels being activated. The work in refs. [28,29] led to questioning the validity of all previous modelling and simulation studies, in which a clean n-level system was assumed, where n is the number of subbands involved in the electron transport process, often with the upper lasing level being the highest level. In refs. [28,29], it was clearly shown that higher-lying leakage channels may be activated at elevated temperatures. Since these works[28,29], our strategy has been to design structures to be as close to a clean n-level system as possible, especially at elevated temperatures. This design strategy has led to the significant increase of T_{max} shown in the present paper.

It is well known in the field of THz QCLs that a diagonal structure, in which the upper- and lower-level wavefunctions are spatially separated, is necessary to reduce the scattering of the hot tail of electron distribution at elevated temperatures and therefore achieve a high T_{max}. However, higher carrier concentrations are then needed to compensate for the reduced oscillator strength in such diagonal structures[30]. These higher doping levels cause significant band bending due to the charging effect—something that was largely ignored previously. A solution to mitigate the adverse charging effect is to relax the double-resonance constraint of the resonant-phonon scheme[31] by using a direct-phonon scheme. In this scheme, depopulation of the lower lasing level takes place by direct longitudinal optical (LO) phonon scattering to a ground state in the same well, without the aid of an extraction level. The direct-phonon depopulation of the lower lasing level is not impacted by the band misalignment caused by higher doping levels, and it has an additional advantage of being insensitive to dephasing caused by interface roughness and impurities. This scheme was explored more than 10 years ago and yielded the simplest QCL structure, involving only two wells per module[32,33]. The achieved T_{max} of ~125 K, however, was far inferior to the state of the art at the time (~186 K), so this approach was not pursued again until recently. By increasing the height of the injection barrier to $Al_{0.3}Ga_{0.7}As$ to block the aforementioned over-the-barrier leakage channel, T_{max} was increased by ~50 K to 173 K (ref. [34]). A similar reduction of thermal leakage led to the successful demonstration of room-temperature operation of a GaAs-based infrared QCL around 9 μm (ref. [35]). In hindsight, after the work in ref. [28], it is clear that carrier leakage over the barriers in those two-well structures is more significant than in the prevailing resonant-phonon structures, because of a much higher bias electric field associated with such a short module. Connecting all the dots, it becomes clear that a direct-phonon scheme based on barriers taller than $Al_{0.15}Ga_{0.85}As$ should be the direction to follow to break the enduring logjam. This has been pursued in several recent reports[27,36,37] as well as in the present work.

Figure 1 shows the subband probability density functions in a QCL with a two-quantum-well active region design. In this scheme, electrons are injected into the upper laser level of the nth module, $|u_n\rangle$, from the injector level of the preceding module, $|i_{n-1}\rangle$, via resonant tunnelling. The lower lasing level in the nth module, $|l_n\rangle$, is depopulated through LO-phonon scattering into a ground state, $|i_n\rangle$, which also serves as the injector level for the next module. The optical gain in the nth module is due to a population inversion between levels $|u_n\rangle$ and $|l_n\rangle$. In this work, the design is focused to achieve a clean three-level system, especially at elevated temperatures. If most of the electrons in the nth module remain within those three levels ($|u_n\rangle$, $|l_n\rangle$ and $|i_n\rangle$), even at elevated temperatures, then, because of its fast depopulation scattering (~0.2 ps), the lower lasing level $|l_n\rangle$ will be much less populated than $|i_{n-1}\rangle$ (which has the same population as $|i_n\rangle$ from periodicity) and $|u_n\rangle$. Accordingly, a large degree of population inversion between $|u_n\rangle$ and $|l_n\rangle$ can be maintained with proper designs. There are two main considerations in designing a clean n-level system like this: reducing intermodule tunnelling except for the desired $|i_{n-1}\rangle \rightarrow |u_n\rangle$ channel and reducing the coupling to higher-lying bound states. Here, we assume that, with the use of tall barriers, the over-the-barrier leakage can be ignored. Following refs. [29,32,34], coupling to higher-lying bound states needs to be significantly reduced to achieve a clean three-level system. The experimental evidence[38] confirms a considerable generation of hot LO phonons in THz QCLs and further validates the importance of such channels.

Accurate knowledge of the band structure (such as conduction band offset and non-parabolicity) is key to minimize parasitic channels, especially those due to undesired intermodule tunnelling. Those details are presented in the Supplementary Information. When the bias is set to align $|i_{n-1}\rangle \rightarrow |u_n\rangle$ (injection alignment), a noticeable spatial overlap exists between those two levels and the higher-energy bound states denoted by $|p_{1,n}\rangle$ and $|p_{2,n}\rangle$, as shown in Fig. 1. At this injection alignment, those higher-energy states form a doublet, which we denote here as $|p_{1,2,n}\rangle$. These states would lie in the continuum for the same scheme with lower barriers[32]. In our band structure engineering, we aimed to minimize the electron-LO-phonon absorption rate into the doublet $|p_{1,2,n}\rangle$ from the $|i_{n-1}\rangle - |u_u\rangle$ levels. This rate depends on the LO-phonon population, the energy separation between $|i_{n-1}\rangle$ and $|p_{1,n}\rangle$ (denoted as $E_{i,pp}$), and the LO-phonon scattering matrix element between the initial and final states. Because the doublet $|p_{1,2,n}\rangle$ is localized, narrower wells will increase the energy separation $E_{i,pp}$, helping to reduce this leakage channel. At the same time, we aimed to maximize the injection strength $|i_{n-1}\rangle \rightarrow |u_n\rangle$, which is quantified in the tight-binding approach by an anticrossing gap, $\Omega_{i,u}$. The tradeoff between reducing leakage channels and increasing the injection rate comprises the main part of the design effort. Exploring in this direction, we designed and grew multiple wafers based on $Al_{0.3}Ga_{0.7}As$ barriers with increasing $\Omega_{i,u}$ and $E_{i,pp}$ and a reducing oscillator strength $f_{i,pp}$. Here, we use the oscillator strength $f_{i,pp}$ as a quantitative benchmark because all scattering mechanisms, including LO-phonon scattering,

Table 1 | Simulation and experimental results of four THz QCLs

Wafer	Growth (date)	$E_{i,pp}$ (meV)	$f_{i,pp}$	$h\nu$ (meV)	$\Omega_{i,u}$ (meV)	J_{max} (kA cm^{-2})	$J_{th}(k)$ (kA cm^{-2})	$f_{u,l}$	T_{max} (K)	Layer sequence (Å)
G528	01/19	54.3	0.25	16.4	1.50	1.60	0.80	0.30	192	**37.4**, 76.4, **16.7**, 154.7
G552	06/19	53.2	0.16	16.0	2.14	2.67	1.48	0.29	235	**33.0**, 76.3, **17.5**, 153.8
G605	08/19	53.0	0.20	15.7	2.41	2.87	1.75	0.30	225	**31.4**, 76.3, **17.5**, 153.1
G652	10/19	58.1	0.14	16.3	2.30	2.60	1.54	0.29	250	**33.7**, 72.0, **18.7**, 144.9

$E_{i,pp}$ is the energy spacing between the injector and doublet $|p_{1,2,n}\rangle$ in Fig. 1, $h\nu$ is the measured lasing frequency, J_{max} is the maximum current density, J_{th} is the threshold current density (in unit of kiloamp per square centimetre (kA cm^{-2}) and $f_{u,l}$ is the oscillator strength between the upper and lower lasing levels, $f_{i,pp}$ is the oscillator strength between $|i-1\rangle$ and $|p_{1,n}\rangle$. The layer sequence starts from the injection barrier. Bold denotes $Al_{0.3}Ga_{0.7}As$ barriers separating GaAs quantum wells. The underline indicates the doped well, with a volume doping of 1.5×10^{17} cm^{-3} in the central 30-Å region. Wafers, which are listed in the first column, are based on the designs TB1WI350-DesA2 (G528), TB1WI356-DesA2V2 (G552), TB1WI356-DesA2V3 (G605) and TB1WI371-DesA2V6 (G652), respectively. The number after 'TB1WI' (which stands for 'tall-barrier 1-well injector') in the design name indicates the number of modules. The number of modules is chosen for ~10 µm of active region.

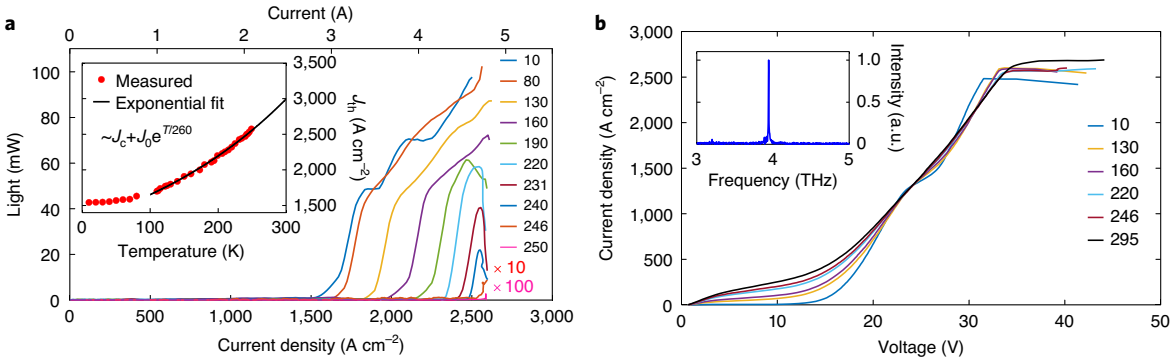

Fig. 2 | Optical and electrical characterization of a device fabricated from wafer G652 with dimensions 1.23 mm × 150 µm, biased with 400-ns pulse width at 500 Hz. a, Plot of THz power versus current density at different temperatures (shown in the colour key, in K). Inset: plot of threshold current density versus temperature (J_{th}–T) with J_c and J_o as fitting parameters. The black line is an exponential fit. **b**, Plot of voltage versus current density (J–V) at different temperatures (shown in the colour key, in K). Inset: a lasing spectrum taken at 246 K. Both the lasing spectrum and light versus current (L–I) curves were measured using a cooled THz photodetector. Note there is no deviation from an exponential fitting in J_{th}–T all the way up to T_{max}, and NDR is preserved at room temperature. Both are telltale signs that there are no significant leakages in the three-level system.

should decrease at the expense of oscillator strength[39] (details are provided in the Supplementary Information). Details of the design and optimization, including other relevant channels (shown as $|u_n\rangle$, $|i_{n-1}\rangle \rightarrow |p_{2,n+1}\rangle$ and $|l_n\rangle \rightarrow |p_{1,n+1}\rangle$ in Fig. 1), are presented in the Supplementary Information. The experimental and simulated results for this optimization process are presented in Table 1.

Figure 2 shows the measured electrical and optical characteristics of a device fabricated from a G652 wafer, which lased up to 250 K, as measured using a cooled THz photodetector. As shown in the inset of Fig. 2a, the plot of J_{th}–T for G652 exhibits no deviation from an exponential increase. Even though exponential J_{th}–T behaviour is purely empirical, in THz QCLs, J_{th} often increases faster than exponentially at the higher end, suggesting leakage channels are activated at those temperatures. The J–V curves in Fig. 2b also show the NDR up to room temperature. The combination of these two features, exponential J_{th}–T and room-temperature NDR, suggests that no significant leakage channels are activated, at least up to T_{max}.

As shown in Table 1, increasing $\Omega_{i,u}$ and $E_{i,pp}$ and reducing $f_{i,pp}$ largely leads to progressive improvement. The only exception is between G605 and G552. Even though G605 and G552 have a similar energy separation with the doublet $|p_{1,2,n}\rangle$ and both show NDR at room temperature, G605 did poorly compared to G552. These two structures were nearly identical, except that the injection barrier was made thinner in G605 to increase the anticrossing gap $\Omega_{i,u}$ so as to increase J_{max} and therefore the gain. However, the injection barrier thickness not only affects the injector anticrossing gap $\Omega_{i,u}$; it also affects the coupling with other parasitic channels denoted by $|p_{1,n+1}\rangle$,$|p_{2,n+1}\rangle$ in Fig. 1. The reasons for the degradation from G552 to G605 appear to be twofold. First, there is an increased coupling between the lower lasing level $|l_n\rangle$ and parasitic channel $|p_{1,n+1}\rangle$ (quantified by anticrossing gap $\Omega_{ln,p_{1,n+1}} > 1$ meV) and a reduced bias separation between this alignment and the injection alignment. Although this channel may appear to help to depopulate the lower lasing level, it introduces additional levels beyond the desired three levels into the transport process and leads to a net detrimental effect. Second, the thinner injection barrier slightly increases the spatial overlap between $|i_{n-1}\rangle$ and $|p_{1,n}\rangle$. As the electron-LO-phonon scattering rate (and other scattering mechanisms) depends on both energy separation and the scattering matrix element, such an increase will increase the scattering rate into the parasitic channel $|p_{1,2,n}\rangle$. These larger leakages may explain the worse performance of G605, which would emphasize the importance of minimizing the involvement of other levels in the transport process and maintaining a clean three-level system. It is worth mentioning that the radiation barrier thickness also plays an important role in the leakage to $|p_{1,2,n}\rangle$. Increasing the radiation barrier thickness can further reduce the leakage to parasitic channels, but it will reduce the oscillator strength and therefore the gain. It is known that the optimum diagonality (quantified by the oscillator strength) is not universal but depends on the specific structure.

Finally, while the T_{max} trends can be explained by design choices, it should be noted that there may be other factors at play. The quality of the underlying molecular beam epitaxy (MBE) growth can impact final device performance, and it remains unclear how significant this effect is. By one key metric—the stability of the superlattice period—we observe exceptionally good growth quality for the top-performing structures in this work with $T_{max} > 220$ K (details are provided in the Supplementary Information). It is possible, then,

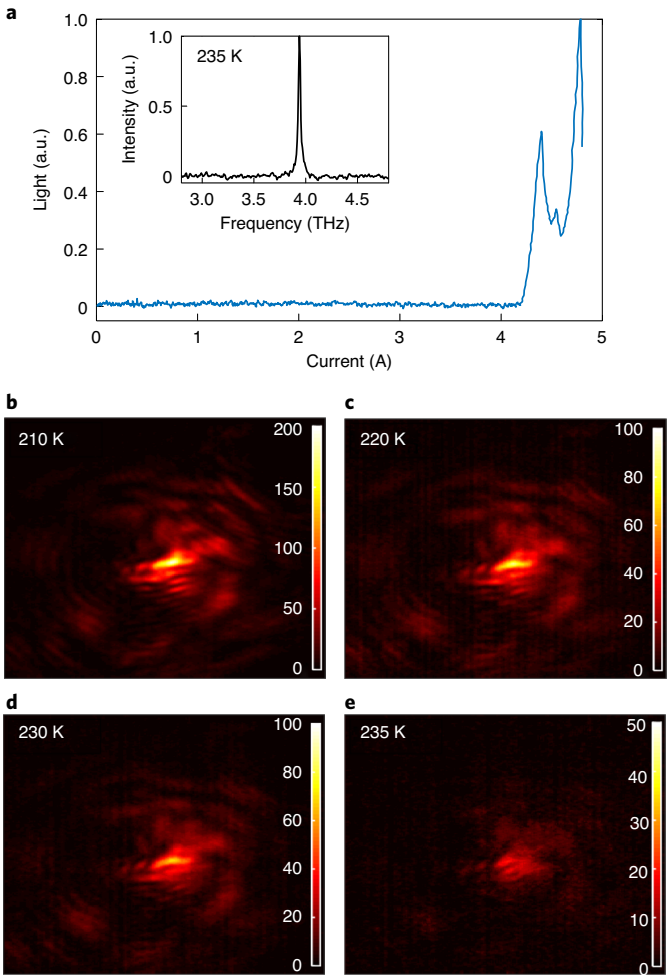

Fig. 3 | Measurements of a TEC-cooled THz QCL device using room-temperature pyroelectric detectors and a THz camera. **a**, Plot of output power versus current. Inset: the lasing spectrum. Both measurements were performed using a single-stage TEC at a temperature of 235 K. The dip in the graph is due to mode hopping in the device. **b**–**e**, Beam pattern images taken with a room-temperature 320 × 240 camera at progressively higher temperatures (210 K (**b**), 220 K (**c**), 230 K (**d**) and 235 K (**e**)) maintained by a three-stage TEC. The false colour indicates the THz radiation intensity. The ripples in the beam pattern are created by a combination of multiple spatial modes created in the Winston cone out-coupler along with diffraction from the subwavelength laser size in the transverse directions.

that there is some correlation between growth stability and T_{max}, although this is clearly not the only factor because the highest T_{max} was achieved in the growth with only second-best stability (G652). We anticipate that both high-quality MBE growth and careful structure design will be essential ingredients for the further development of high-performance THz QCLs.

The high-temperature performance of G652, which far exceeds the decade-old record of 225 K achieved with an impractically strong magnetic field (up to 30 T)[40], opens the door to applications that were previously unattainable. A maximum lasing temperature around 196–210 K has already enabled the use of compact and portable thermoelectric coolers (TECs)[27,41] instead of bulky cryogenics. However, as T_{max} gets close to the cooling floor of a multistage TEC, the output power is not sufficient for real-time imaging applications. In the present work, the maximum operating temperature has been increased significantly to 250 K. Importantly for applications, this high T_{max} yields much greater average output powers in the range ~210–235 K, which is the cooling range of commercial TECs. This enables compact THz lasers with sufficient power for real-time imaging and fast spectral measurements using room-temperature cameras and detectors.

To demonstrate this, we operated a QCL based on G652 at 235 K, cooled by a single-stage commercial TEC. The laser was operated in pulsed mode (1% duty cycle, 100-ns pulse at 100 kHz) and it generated ~2 W of heat. By using a TEC module with only one stage, the entire assembly could be kept small. At the same time, it cooled the laser enough that it could supply a sufficient level of output power to perform fast spectral measurements without requiring an especially high-performance detector. The lasing spectrum of this single-stage TEC-cooled laser was measured using a pyroelectric detector with a noise-equivalent power of ~460 pW $Hz^{-1/2}$, and with only several seconds of integration time. The *L*–*I* curve was also measured using the same detector, as shown in Fig. 3a. Using these high-temperature THz QCLs, following the work[42] that was performed with a thermomechanical cooler at 33 K, we have also demonstrated a portable THz imaging system. Real-time imaging measurements using a THz camera (manufactured by NEC with a noise-equivalent power in the range of ~50 pW $Hz^{-1/2}$) require much higher average power levels than the spectral measurements. Thus, a three-stage TEC was used—housed in the same vacuum chamber but with an external single-stage TEC module—to achieve a 2-W heat removal capacity down to 210 K. The average output power was sufficient that the laser beam could be imaged with a 320 × 240 THz focal-plane array camera with 32-frame averaging (integration time ~2 s). The captured beam patterns are shown in Fig. 3b–e at different operating temperatures from 210 K to 235 K.

In conclusion, by carefully designing QCL structures to reduce carrier leakage channels at elevated temperatures, we have developed THz QCLs (at ~4 THz) with a maximum operating temperature of T_{max} = 250 K. This operating temperature enabled the construction of coherent THz radiation sources using commercial (less than $100) single- and multi-stage TECs, yet with power levels sufficient for real-time imaging of the beam pattern and fast spectral measurements without requiring expensive cryogenically cooled detectors. The combination of TEC-cooled THz QCLs with room-temperature cameras and detectors enables portable systems that are operable outside the laboratory environment. Furthermore, and perhaps more importantly in the long term, the demonstrated significant increase in T_{max} and the preservation of room-temperature NDR indicate a clear path towards further increases in T_{max} by designing clean *n*-level systems based on the direct-phonon scheme with tall barriers.

Online content

Any methods, additional references, Nature Research reporting summaries, source data, extended data, supplementary information, acknowledgements, peer review information; details of author contributions and competing interests; and statements of data and code availability are available at https://doi.org/10.1038/s41566-020-00707-5.

Received: 16 April 2020; Accepted: 22 September 2020;
Published online: 2 November 2020

References

1. Mittleman, D. M. Twenty years of terahertz imaging. *Opt. Express* **26**, 9417–9431 (2018).
2. Korter, T. & Plusquellic, D. F. Continuous-wave terahertz spectroscopy of biotin: vibrational anharmonicity in the far-infrared. *Chem. Phys. Lett.* **385**, 45–51 (2004).
3. Ogawa, Y., Hayashi, S., Oikawa, M., Otani, C. & Kawase, K. Interference terahertz label-free imaging for protein detection on a membrane. *Opt. Express* **16**, 22083–22089 (2008).

4. Kidd Walker, C. et al. *GUSTO: Gal/Xgal U/LDB Spectroscopic-Stratospheric TeraHertz Observatory* Abstract 231 (American Astronomical Society, 2018).
5. Rezac, L. et al. First detection of the 63-μm atomic oxygen line in the thermosphere of Mars with GREAT/SOFIA. *A&A* **580**, L10 (2015).
6. Federici, J. F. et al. THz imaging and sensing for security applications—explosives, weapons and drugs. *Semicond. Sci. Technol.* **20**, 266–280 (2005).
7. Duling, I. & Zimdars, D. Terahertz imaging: revealing hidden defects. *Nat. Photon.* **3**, 630–632 (2009).
8. Rahman, A., Rahman, A. K. & Rao, B. Early detection of skin cancer via terahertz spectral profiling and 3D imaging. *Biosens. Bioelectron.* **82**, 64–70 (2016).
9. Cheon, H. et al. Detection and manipulation of methylation in blood cancer DNA using terahertz radiation. *Sci. Rep.* **9**, 6413 (2019).
10. Köhler, R. et al. Terahertz semiconductor-heterostructure laser. *Nature* **417**, 156–159 (2002).
11. Siles, J. V. et al. A new generation of room-temperature frequency-multiplied sources with up to 10× higher output power in the 160-GHz–1.6-THz range. *IEEE Trans. Terahertz Sci. Technol.* **8**, 596–604 (2018).
12. Imran, M. et al. THz diode technology: status, prospects and applications. *Proc. IEEE* **105**, 990–1007 (2017).
13. McIntosh, K. A. et al. Terahertz photomixing with diode lasers in low-temperature-grown GaAs. *Appl. Phys. Lett.* **67**, 3844 (1995).
14. Belkin, M. A. et al. Terahertz quantum-cascade-laser source based on intracavity difference-frequency generation. *Nat. Photon.* **1**, 288–292 (2007).
15. Lu, Q. Y. et al. Continuous operation of a monolithic semiconductor terahertz source at room temperature. *Appl. Phys. Lett.* **104**, 221105 (2014).
16. Berry, C. W., Hashemi, M. R. & Jarrahi, M. Generation of high-power pulsed terahertz radiation using a plasmonic photoconductive emitter array with logarithmic spiral antennas. *Appl. Phys. Lett.* **104**, 081122 (2014).
17. Singh, A. et al. Up to 70-THz bandwidth from an implanted Ge photoconductive antenna excited by a femtosecond Er:fibre laser. *Light Sci. Appl.* **9**, 30 (2020).
18. Wilke, I. & Suranjana, S. in *Terahertz Spectroscopy* (ed. Dexheimer, S. L.) 59–90 (CRC Press, 2017).
19. Curwen, C. A., Reno, J. L. & Williams, B. S. Terahertz quantum cascade VECSEL with watt-level output power. *Appl. Phys. Lett.* **113**, 011104 (2018).
20. Jin, Y., Reno, J. L. & Kumar, S. Phase-locked terahertz plasmonic laser array with 2-W output power in a single spectral mode. *Optica* **7**, 708–715 (2020).
21. Khalatpour, A., Reno, J. L., Kherani, N. P. & Hu, Q. Unidirectional photonic wire laser. *Nat. Photon.* **11**, 555–559 (2017).
22. Burghoff, D. et al. Terahertz laser frequency combs. *Nat. Photon.* **8**, 462–467 (2014).
23. Rösch, M., Scalari, G., Beck, M. & Faist, J. Octave-spanning semiconductor laser. *Nat. Photon.* **9**, 42–47 (2015).
24. Kao, T. Y., Reno, J. L. & Hu, Q. Amplifiers of free-space terahertz radiation. *Optica* **4**, 713–716 (2017).
25. Williams, B. S., Kumar, S., Hu, Q. & Reno, J. L. Operation of terahertz quantum-cascade lasers at 164 K in pulsed mode and at 117 K in continuous-wave mode. *Opt. Express* **13**, 3331–3339 (2005).
26. Fathololoumi, S. et al. Terahertz quantum cascade lasers operating up to ~200 K with optimized oscillator strength and improved injection tunneling. *Opt. Express* **20**, 3866–3876 (2012).
27. Bosco, L. et al. Thermoelectrically cooled THz quantum cascade laser operating up to 210 K. *Appl. Phys. Lett.* **115**, 010601 (2019).
28. Albo, A. & Hu, Q. Carrier leakage into the continuum in diagonal GaAs/$Al_{0.15}$GaAs terahertz quantum cascade lasers. *Appl. Phys. Lett.* **107**, 241101 (2015).
29. Albo, A., Hu, Q. & Reno, J. L. Room temperature negative differential resistance in terahertz quantum cascade laser structures. *Appl. Phys. Lett.* **109**, 081102 (2016).
30. Chan, C. W. I., Albo, A., Hu, Q. & Reno, J. L. Tradeoffs between oscillator strength and lifetime in terahertz quantum cascade lasers. *Appl. Phys. Lett.* **109**, 201104 (2016).
31. Williams, B. S., Callebaut, H., Kumar, S., Hu, Q. & Reno, J. L. 3.4-THz quantum cascade laser based on LO-phonon scattering for depopulation. *Appl. Phys. Lett.* **82**, 1015 (2003).
32. Kumar, S., Chan, C. W. I., Hu, Q. & Reno, J. L. Two-well terahertz quantum-cascade laser with direct intrawell-phonon depopulation. *Appl. Phys. Lett.* **95**, 141110 (2009).
33. Scalari, G. et al. Broadband THz lasing from a photon–phonon quantum cascade structure. *Opt. Express* **18**, 8043–8052 (2010).
34. Albo, A., Flores, Y. V., Hu, Q. & Reno, J. L. Two-well terahertz quantum cascade lasers with suppressed carrier leakage. *Appl. Phys. Lett.* **111**, 111107 (2017).
35. Page, H. et al. 300-K operation of a GaAs-based quantum-cascade laser at $\lambda \approx 9$ μm. *Appl. Phys. Lett.* **78**, 3529–3531 (2001).
36. Franckié, M. et al. Two-well quantum cascade laser optimization by non-equilibrium Green function modeling. *Appl. Phys. Lett.* **112**, 021104 (2018).
37. Franckié, M. & Jérôme, F. Bayesian optimization of terahertz quantum cascade lasers. *Appl. Phys. Appl.* **13**, 034025 (2020).
38. Vitiello, M. S. et al. Non-equilibrium longitudinal and transverse optical phonons in terahertz quantum cascade lasers. *Appl. Phys. Lett.* **100**, 091101 (2012).
39. Faist, J. *Quantum Cascade Lasers* (Oxford Univ. Press, 2013).
40. Wade, A. et al. Magnetic-field-assisted terahertz quantum cascade laser operating up to 225 K. *Nat. Photon.* **3**, 41–45 (2009).
41. Kainz, A. M. et al. Thermoelectric-cooled terahertz quantum cascade lasers. *Opt. Express* **27**, 20688–20693 (2019).
42. Lee, A. W. M., Williams, B. S., Kumar, S., Hu, Q. & Reno, J. L. Real-time imaging using a 4.3-THz quantum cascade laser and a 320×240 microbolometer focal-plane array. *IEEE Photon. Technol. Lett.* **18**, 1415–1417 (2006).

Methods
Methods are included in the Supplementary Information.

Data availability
The data that support the plots within this paper and other findings of this study are available from the corresponding author upon reasonable request.

Acknowledgements
We thank A. Lee and W. Kao at LongWave Photonics for the loan of the NEC THz camera. This work is supported by National Aeronautics and Space Administration (NASA), the Canada First Research Excellence Fund and the Natural Sciences and Engineering Research Council of Canada (NSERC).

Author contributions
A.K. developed the simulation and optimization codes, designed and fabricated the lasers and performed the measurements. The single-stage TEC chamber was designed by A.K. and further improved by A.K.P. A.K.P. optimized the multistage TEC set-up and performed the real-time imaging with a THz camera and spectral measurements using a pyroelectric detector. C.D. performed MBE growth and optimization of growth conditions, as well as MBE related material characterization, under the supervision of Z.R.W. The project was supervised by Q.H., who was also involved in the design and formulated the design strategy of clean n-level systems for the QCL structures. A.K. and Q.H. wrote the paper with editing help from C.D. and Z.R.W. A.K.P. wrote the TEC section in the Supplementary Information. C.D. and Z.R.W. wrote the MBE growth details in the Supplementary Information.

Competing interests
The authors declare no competing interests.

Additional information
Supplementary information is available for this paper at https://doi.org/10.1038/s41566-020-00707-5.

Correspondence and requests for materials should be addressed to Q.H.

Reprints and permissions information is available at www.nature.com/reprints.